

THE THERMAL STRUCTURE OF THE CIRCUMSTELLAR DISK SURROUNDING THE CLASSICAL BE STAR γ CASSIOPEIA

T. A. A. SIGUT & C. E. JONES

DEPARTMENT OF PHYSICS AND ASTRONOMY, THE UNIVERSITY OF WESTERN ONTARIO, LONDON, ONTARIO, N6A 3K7, CANADA

Accepted for Publication by The Astrophysical Journal

ABSTRACT

We have computed radiative equilibrium models for the gas in the circumstellar envelope surrounding the hot, classical Be star γ Cassiopeia. This calculation is performed using a code that incorporates a number of improvements over previous treatments of the disk's thermal structure by Millar & Marlborough (1998) and Jones, Sigut & Marlborough (2004); most importantly, heating and cooling rates are computed with atomic models for H, He, CNO, Mg, Si, Ca, & Fe and their relevant ions. Thus, for the first time, the thermal structure of a Be disk is computed for a gas with a solar chemical composition as opposed to assuming a pure hydrogen envelope. We compare the predicted average disk temperature, the total energy loss in H α , and the near-IR excess with observations and find that all can be accounted for by a disk that is in vertical hydrostatic equilibrium with a density in the equatorial plane of $\rho(R) \approx 3$ to $5 \cdot 10^{-11} (R/R_*)^{-2.5} \text{ g cm}^{-3}$. We also discuss the changes in the disk's thermal structure that result from the additional heating and cooling processes available to a gas with a solar chemical composition over those available to a pure hydrogen plasma.

Subject headings: stars: circumstellar matter – stars: emission line, Be – stars: individual: γ Cas

1. INTRODUCTION

Classical Be stars are non-supergiant B stars that possess circumstellar material in the form of an equatorial disk. While the circumstellar disk is almost certainly a decretion disk of material from the star's atmosphere, the detailed mechanism that creates and maintains such a disk remains unclear (Porter & Rivinus 2003; Owocki 2004). Rapid rotation of the central B star seems to play an important role, but there is still considerable debate as to the extent (Townsend et al. 2004; Fremat et al. 2005). Historically, the observational evidence for such circumstellar material has been either spectroscopic or polarimetric in nature, and the accepted observational definition of a Be star has been the appearance (at the current or previous epoch) of emission in the hydrogen Balmer lines. It has been recognized since the days of Struve (1931) that recombination in a flattened disk could reproduce the range of spectroscopically observed H α profiles. In addition, the net (continuum) linear polarization observed in Be stars is well explained by electron scattering from non-spherically distributed circumstellar gas (Coyne & Kruszewski 1969; Waters & Marlborough 1992).

Beginning with the resolution of ϕ Persei (B2 Vpe) at radio wavelengths with the Very Large Array by Dougherty & Taylor (1992), interferometry has increasingly been used to spatially resolve circumstellar material. Be star disks have been resolved at radio, near-IR, and optical wavelengths, with these observations conclusively revealing the disk (Quirrenbach et al. 1993, 1997; Tycner et al. 2005, 2006). The observations are consistent with the suggestion of Poeckert & Marlborough (1978) that Be star disks are geometrically quite thin with opening angles of only a few degrees.

Currently, optical interferometric observations require theoretical models of the emitting region in order to

interpret the observed visibilities. Often observers fit simple models with free parameters to the data to describe the disk emissivity. However, this simple procedure can be considerably improved by using a detailed model for the thermal structure of the Be star disk. Such models naturally predict the emissivity and opacity of the gas required to produce theoretical spectroscopic images (Millar & Marlborough 1998; Jones, Sigut & Marlborough 2004; Carciofi & Bjorkman 2006).

γ Cassiopeia (HD 5394; B0 IVe) is a interesting classical Be star which has a dense, cool, equatorial disk (Millar & Marlborough 1998). This disk has been resolved with optical interferometry (Stee et al. 1995; Tycner et al. 2005). γ Cas is likely the primary in a binary system (Harmanec et al. 2000; Miroshnichenko et al. 2002) and has unique X-ray characteristics (Smith et al. 2004). Although γ Cas is often quoted as “the prototypical” Be star, it has become clear that it possesses some unique characteristics. Nevertheless, it is a well-studied star making it an appropriate choice to test new codes and compare results with previously published work. In this current paper, we extend the radiative-equilibrium models of Millar & Marlborough (1998) and Jones, Sigut & Marlborough (2004) for the early Be star γ Cas to a disk models with a solar chemical composition.

2. CALCULATIONS

2.1. Overview

The calculations in this paper were performed with a new code, BEDISK, which is loosely based upon the calculational approach of Millar & Marlborough (1998) and Jones, Sigut & Marlborough (2004). Models for the circumstellar material were constructed assuming a density distribution falling as an R^{-n} power-law in the equatorial plane, following the models of Waters (1986),

Coté & Waters (1987), and Waters et al. (1987). By comparing to observations of the infrared excesses of Be stars, these authors found power-law density exponents in the range $n \approx 2.0$ to 3.5. Perpendicular to the equatorial plane, it was assumed that the gas is in vertical, isothermal, hydrostatic equilibrium. Given the disk density distribution and the photoionizing radiation field from the central star, the equations of statistical equilibrium were solved for the ionization state and level populations of H, He, CNO, Mg, Si, Ca, and Fe subject to the constraints of charge and particle conservation. Radiative transfer was handled via the escape probability approximation, and it was assumed that the dominant escape route for photons was perpendicular to the exponentially stratified disk. From this solution, the rates of energy gain and energy loss at each computational grid point were obtained, and the local temperatures were iteratively adjusted to enforce radiative equilibrium.

The main features and assumptions of this code are now discussed in detail.

2.2. The BEDISK Code

The circumstellar disk was assumed to be axisymmetric about the star's rotation axis and symmetric about the mid-plane of the disk. In all that follows, R is used for the radial distance from the star's rotation axis and Z , for the perpendicular height above the equatorial plane. Thus the cylindrical co-ordinates of any disk location are (R, Z) . If R_* denotes the stellar radius, then the calculation domain is $R_* \leq R_i \leq R_{\max}$ with $i = 1 \dots n_r$, and $0 \leq Z_j \leq Z_{\max}(R_i)$ with $j = 1 \dots n_z$. Typically, n_r is set to 60 with $R_{\max}/R_* = 50$, and n_z is set to 40.

The code accepts a user-defined set of atomic models which list the energy levels and the bound and free radiative and collisional transitions for each atom and ion to be included in the calculation. The set of atoms and ions and the total number of atomic levels and radiative transitions used for the current calculations are listed in Table 1. For this initial work, the number of energy levels included for each atom and ion is similar to the list of energy levels given by Moore & Merrill (1968). Sources for the required atomic data are given in Appendix A. The abundances assumed for the various elements can be found in Table 2 and are taken from the accepted solar abundances of Anders & Grevesse (1989) and Anders & Noels (1993).

The number of atomic levels included for each atom/ion in Table 1 is fairly modest, although large enough to include most of the collisionally-excited lines seen in the optical and UV spectra of Be stars. While non-LTE solutions can be sensitive to the number of atomic levels included (see, for example, Sigut (1996) for a case-study of C II in B stars), the computational time also increases sharply with the number of levels. Table 1 represents a compromise between realism and computational efficiency. Several techniques exist to group atomic levels into "super-levels" (see, for example, Hubeny, Hummer, & Lanz 1994) which will allow future work to utilize more complete atomic models.

The density structure of the disk is chosen in an ad-hoc manner. All calculations assume that the density drops as an R^{-n} power-law in the equatorial plane, and at each R , the gas is in vertical, isothermal hydrostatic equilibrium. To obtain the density above the equatorial

TABLE 1
ATOMIC MODELS

Z	Atom	Number of Levels	Transitions
1	H I	15	77
1	H II	1	0
2	He I	13	16
2	He II	1	0
6	C I	15	23
6	C II	10	20
6	C III	21	45
6	C IV	8	15
6	C V	1	0
7	N I	23	51
7	N II	15	24
7	N III	10	20
7	N IV	1	0
8	O I	15	19
8	O II	29	80
8	O III	15	24
8	O IV	10	19
8	O V	1	0
12	Mg I	17	28
12	Mg II	12	25
12	Mg III	1	0
14	Si I	37	109
14	Si II	8	13
14	Si III	18	27
14	Si IV	11	23
14	Si V	1	0
20	Ca I	24	42
20	Ca II	11	20
20	Ca III	1	0
26	Fe I	40	90
26	Fe II	39	191
26	Fe III	1	0
	TOTAL	425	1001

TABLE 2
ELEMENTAL ABUNDANCES

Element	Abundance ^a
H	12.00
He	10.90
C	8.55
N	7.97
O	8.87
Mg	7.58
Si	7.55
Ca	6.36
Fe	7.51

^a The tabulated is abundance is $\log(N/N_{\text{H}}) + 12$.

plane at each radial distance, the user supplies a fixed set of density-drops from the equatorial plane,

$$d_j \equiv \ln\{\rho(Z_j)/\rho(Z_j = 0)\} \quad (1)$$

for $j = 1 \dots n_z$. Here $d_1 = 0$ by definition, and $d_{n_z} \equiv -4$. Then the Z_j at which this density drop would occur, given the current value of R_i , is computed assuming vertical hydrostatic equilibrium with an isothermal temperature T_o ,

$$\frac{Z_j}{R_i} = \left\{ \left(\frac{\alpha/R_i}{d_j + \alpha/R_i} \right)^2 - 1 \right\}^{\frac{1}{2}}. \quad (2)$$

Here α is given by

$$\alpha = \frac{\mu m_H}{k T_o} GM, \quad (3)$$

where μ is the mean-molecular weight, ≈ 0.5 for an ionized, pure hydrogen disk, and M is the mass of the central B-star. Thus the density at (R_i, Z_j) is given by

$$\rho(R_i, Z_j) = \rho_0 \left(\frac{R_i}{R_*} \right)^{-n} d_j. \quad (4)$$

In this expression, ρ_0 , n , and T_o (through equation 3) are the parameters which define the density structure of the disk.

At each computational grid point, the photoionizing radiation field is required to evaluate the photoionization rates of all atoms/ions for the statistical equilibrium equations and to compute the photoionization heating rates for the radiative equilibrium solution. It is usual to divide this radiation field into a direct and diffuse contribution,

$$J_\nu = J_\nu^{\text{Dir}} + J_\nu^{\text{Dif}}. \quad (5)$$

The direct contribution represents the radiation from the central star while the diffuse contribution arises from the disk. Note that despite this division, the only energy input into the circumstellar disk is assumed to be from the star itself so that ultimately, the energy in the diffuse field has its origin in direct radiation from the star.

There is some evidence that γ Cas has a binary companion with an orbital period of ~ 200 days (Harmanec et al. 2000; Miroshnichenko et al. 2002). However, the exact orbit and the nature of the companion, including its spectral type and luminosity, are unknown. Rather than introduce further uncertain parameters into the calculation (and invalidate the axisymmetric geometry), we shall assume that the energy input into the disk of γ Cas from any potential companion is negligible.

The direct component from the central star to the photoionizing radiation field at grid location (R_i, Z_j) is given by

$$J_\nu^{\text{Dir}}(R_i, Z_j) = \int_{\Omega_*} I_{\mu\nu}(R_i, Z_j, \hat{n}) d\Omega \quad (6)$$

where $d\Omega$ is an infinitesimal patch of solid angle centred around the direction \hat{n} . The integral is over the visible stellar surface. Typically the surface is divided into a few hundred patches and the transfer equation is solved along a ray from the centre of each patch to the grid location¹. The radiation field at the stellar surface was taken from an LTE stellar atmosphere of Kurucz (1993) which specified the mean intensity, $J_\nu(\tau_\nu = 0)$, at the top of the photosphere over a grid of 1221 frequencies. This was turned into the required intensity at each surface element by using the limb-darkening law

$$I_{\mu\nu} = I_o \{1 - a_\nu(1 - \mu) - b_\nu(1 - \mu)^2\} \quad (7)$$

where the coefficients a_ν and b_ν were linearly interpolated from Table V of Wade & Rucinski (1985). Here μ is the

¹ By choosing to solve the transfer equation along these rays, as opposed to simply applying exponential extinction of the stellar photospheric intensity, some contribution of the diffuse field is included.

usual cosine of the surface viewing angle. Computing the mean intensity from this expression and setting it to the LTE model atmosphere prediction, we find that

$$I_o = \frac{J_\nu(\tau_\nu = 0)}{1 - a_\nu - (3/4)b_\nu}. \quad (8)$$

While this procedure is approximate, and the exact $I_{\mu\nu}$ for each μ predicted by the LTE model could have been used, this approximation seems commensurate with others made in the construction of these models. We also note the use of a more physically realistic non-LTE, line-blanketed atmosphere for $J_\nu(\tau_\nu = 0)$ would be a useful future improvement.

In addition to limb darkening, gravity darkening induced by rapid stellar rotation can change the intensity distribution across the stellar disk and hence modify the direct component to the photoionizing radiation field. Tycner et al. (2005) interferometrically resolved γ Cas's disk and estimated its inclination angle to the sky. They conclude the γ Cas rotates at 0.7 ± 0.1 of its critical velocity. As γ Cas does not seem to rotate particularly close to its critical velocity, we have not included gravity darkening (and the associated geometrical distortion of its surface) into the calculation of the direct photoionizing radiation field. This point is further discussed in Section 3.1 where the adopted stellar parameters for γ Cas are discussed.

The simplest treatment for the diffuse field is to employ the on-the-spot (OTS) approximation in which the recombination rate to level n of hydrogen is written as

$$R_{\kappa,n}^H(\tau_n) \equiv R_{\kappa,n}^H e^{-\tau_n}. \quad (9)$$

Here τ_n is the optical depth at the continuum limit for photoionization from level n along a vertical ray to the nearest edge of the disk (this is consistent with our assumption that the dominant photon escape route is perpendicular to the disk —see later discussion). Thus the principle assumption of the OTS approximation is that at high continuum optical depths, $\tau_n \gg 1$, recombination to level n produces a photon that is locally absorbed within the same volume element, essentially undoing the recombination. Including the continuum optical depth dependence in equation (9) ensures that the OTS approximation is used only when $\tau_n \gg 1$; the full recombination coefficient is employed when the gas becomes optically thin in the continuum. We have applied to OTS approximation only to recombination to level $n = 1$ in hydrogen. The optical depths in the remaining continua are typically not large enough for a significant effect. We discuss a more complex, but still approximate, treatment for the diffuse field in section 3.5.

Given the photoionizing radiation field and current estimates of the electron temperature and electron density at each grid location, we solve the statistical equilibrium equations to obtain the level populations for all atoms and ions. For atom k , and all of its associated ions, these are

$$\sum_{j \neq i}^{N_L^k} n_i^k R_{ij} - \sum_{j \neq i}^{N_L^k} n_j^k R_{ji} = 0, \quad (10)$$

for $i = 1, \dots, N_L^k$ where N_L^k is the number of atomic levels included for the k^{th} atom and its ionization stages. Note

that these equations must be supplemented by a particle conservation equation of the form

$$\sum_i^{N_L^k} n_i^k = 10^{A_k-12} n_H \quad (11)$$

for each atomic species. The elemental abundance, A_k , can be found from Table 2.

In the case of bound-bound transitions $i \rightarrow j$, $i < j$, the rates have the simple form

$$R_{ij} = n_e q_{ij}(T_e) \quad (12)$$

and

$$R_{ji} = A_{ji} P_{\text{esc}}(\tau_z) + n_e q_{ji}(T_e). \quad (13)$$

Here the factors $q_{ij}(T_e)$ and $q_{ji}(T_e)$ represent collisional excitation and de-excitation respectively and are proportional to the Maxwellian-averaged collision strength for $i \rightarrow j$ transition. A_{ji} is the usual Einstein transition probability for spontaneous emission. This form of the statistical equilibrium equations handles radiative transfer in the line via the escape-probability approximation. The escape probability for each grid location was obtained by computing the line-centre optical depth to the nearest vertical edge of the disk (denoted τ_z) and then using this optical depth to estimate the static, single-flight escape probability assuming complete redistribution in the spectral line.

We have assumed that the dominant loss route for photons is perpendicular to the disk because of the exponential density stratification implied by vertical hydrostatic equilibrium. As it is reasonable to assume that the main motion of the disk gas is Keplerian rotation about the central star, the Doppler shifts experienced by photons escaping roughly perpendicular to the disk will be small, and it is appropriate to approximate the escape probability, $P_{\text{esc}}(\tau_z)$, by a *static*, single-flight escape probability, as opposed to employing the Sobolev approximation. This is consistent with the definition of τ_z as the optical along a ray perpendicular to the disk to the nearest edge; τ_z is not defined in terms of a local velocity gradient as in the Sobolev approximation.

The form of the static, single-flight escape probability appropriate for complete-redistribution over a Doppler profile is

$$P_{\text{esc}}(\tau) = \frac{1}{4\tau (\ln(\tau/\sqrt{\pi}))^{1/2}}, \quad (14)$$

where $\tau \gg 1$ (Mihalas 1978; Cannon 1985). As this result is an asymptotic expansion (essentially in the limit that the scale of variation of the line source function is large compared to the width of the scattering kernel – see Cannon 1985), an ad-hoc correction is needed to handle $\tau \ll 1$. Here we have adopted the suggestion of Tielens (2005) where the escape probability is taken to be

$$P_{\text{esc}}(\tau) = \frac{1 - e^{-2.34\tau}}{4.68\tau}, \quad (15)$$

for $\tau < 7$. This function is continuous with the asymptotic result at $\tau = 7$ and tends to the limit of $1/2$ as $\tau \rightarrow 0$, a reasonable result if the collisional destruction probability of the line photon upon scattering is not too small.

In the case $i \rightarrow j \equiv \kappa$ is a bound-free transition, the photoionization and recombination (spontaneous plus stimulated) rates are given by

$$R_{i\kappa} = 4\pi \int_{\nu_o}^{\infty} \sigma_{i\kappa}(\nu) J_\nu \frac{d\nu}{h\nu} \quad (16)$$

and

$$R_{\kappa i} = 4\pi \left(\frac{n_i}{n_\kappa} \right)^* \int_{\nu_o}^{\infty} \sigma_{i\kappa}(\nu) \left(\frac{2h\nu^3}{c^2} + J_\nu \right) \frac{d\nu}{h\nu}. \quad (17)$$

Here $(n_i/n_\kappa)^*$ is the LTE population ratio found from the Saha-Boltzmann equation and it is proportional to the electron density, n_e (Mihalas 1978). Dielectronic recombination and autoionization are included by retaining the full resonance structure of the photoionization cross section $\sigma_{i\kappa}(\nu)$.

Given the solution for the atomic level populations, a new estimate for the electron density can be made by enforcing charge conservation, and the rates of heating and cooling for the various atomic processes can then be computed. Heating includes photoionization and collisional de-excitation while cooling includes radiative recombination and collisional excitation. Detailed expressions for all of these processes can be found in Osterbrock (1989). However, in contrast to Osterbrock (1989), transitions (and the implied cooling) due to radiative recombination were computed explicitly via equation (17) for each atomic level; total recombination co-efficients (summed over n) were not used.

Heating due to viscous dissipation in a Keplerian disk was also included (Lee, Saio, & Osaki 1991) but was always found to be negligible.

Net cooling due to free-free emission (in the fields of H I and He II) was included via the expression of Rybicki & Lightman (1979), modified as suggested by Netzer (1990) to account for the reduction in the free-free cooling rate as the gas becomes optically thick to free-free radiation,

$$L_{\text{ff}} = 1.4 \cdot 10^{-27} \sqrt{T_e} n_e \sum_{i=\text{H,He}} n_i Z_i^2 \bar{g}_{\text{ff}} e^{-h\nu_{\text{max}}/kT_e}. \quad (18)$$

Here $Z_i = 1$ and the frequency cut-off, ν_{max} , suggested by Netzer (1990), is the smallest frequency for which the optical depth to the nearest edge of the disk exceeds one. The Gaunt factor, \bar{g}_{ff} , which varies slowly with temperature, was set to a constant value of 1.2 which Rybicki & Lightman (1979) indicate will approximate the exact result to within 20%.

To find the equilibrium kinetic temperature, T_e , at each grid location, heating and cooling were balanced by searching for a zero in the net-cooling rate, $\eta_C(T_e)$. The root was initially located via bisection and then refined with the secant method. In the rare case of multiple roots, the stable one satisfying $d\eta_C/dT_e > 0$ was chosen.

The overall flow of the calculation is to start at the inner boundary of the disk, closest to the star at $i = 1$. Solutions proceed downward in Z , from the top of the disk ($j = n_z$) to the equatorial plane ($j = 1$). This allows the optical depths back to the star and to the nearest edge of the disk to be kept current with the solution level populations.

3. COMPUTATIONS

In this section, we first compare the predictions of our code with known results for γ Cas. Next we explore a wide range of disk parameters for γ Cas and investigate the effect on the temperature structure of the disk of using a solar chemical composition for the gas. We then examine the energy loss in the spectral lines included in the models and compute the near infrared spectral energy distribution. Finally, we examine the computation of the diffuse photoionizing radiation field generated by the disk itself in order to evaluate the use of the OTS approximation for most of the models computed in this work.

3.1. Comparison with Millar & Marlborough

Millar & Marlborough (1998) constructed a pure-hydrogen radiative equilibrium model for γ Cas. Millar & Marlborough (1999) (MM, hereafter) extended this work to include the OTS approximation for the diffuse radiation field, and it is this temperature distribution which we have chosen for comparison. We adopt the same stellar parameters for γ Cas as MM, which are reproduced in Table 3. As we use these fundamental parameters for all of the calculations in this work, some additional comment is in order, particularly concerning the adopted stellar effective temperature. Fremat et al. (2005) investigate the effect of rapid rotation on fundamental parameter determinations of B stars. They find, by fitting the line spectrum between 4250 and 4500 Å, “apparent stellar parameters” for γ Cas (those obtained by a best fit classical, plane-parallel model atmosphere) of $T_{\text{eff}} = 26,400$ K and $\log(g) = 3.8$ which are close to the parameters adopted in this work. Nevertheless, they do find significant effects of rotation in their best-fit rotating models which have a *parent non-rotating counterpart* T_{eff} (see their paper for details) of $\approx 30,000$ K. This result suggests that accounting for the rotation of γ Cas in a manner following Fremat et al. (2005) (but using non-LTE stellar atmospheres) would be a useful future improvement in the computation of the direct stellar contribution to the photoionizing radiation field.

The fixed density structure for the γ Cas disk adopted by MM is described by Marlborough (1969) and is slightly different from the model described in section 2.2. MM assume that the disk is in isothermal, hydrostatic equilibrium at only one radial distance from the central star and that the radial drop-off in the equatorial density follows from an assumed (radial) outflow velocity law and the equation of continuity. We have simply adopted the (R_i, Z_j) grid of MM (which is 24 by 20) and their total density at each grid point as input to BEDISK. We have used a 5-level hydrogen atom plus continuum for this comparison and have also used the OTS approximation (as described previously) for the diffuse field. Despite this, there are still some significant differences between the calculations: our approach uses the optical depths in the OTS approximation and in the line escape probabilities as opposed to the various cases of MM. We use a newer ATLAS stellar atmosphere to predict the photoionizing radiation field from the star and use many more rays from each grid point back to the star. No attempt was made to use identical atomic data: MM included collisional transitions for only transitions n to

TABLE 3
STELLAR PARAMETERS FOR γ CAS.

Parameter	Value	Unit
Spectral Class	B0 IVe	...
Radius	10.0	R_{\odot}
Mass	17.0	M_{\odot}
Luminosity	$3.4 \cdot 10^4$	L_{\odot}
T_{eff}	25,000	K
$\log(g)$	3.50	cm s^{-2}
Distance ^a	188_{-18}^{+22}	pc

^a Distance from the Hipparcos catalogue (Perryman et al. 1997).

$n \pm 1$ in hydrogen whereas we have included all collisional rates. Nevertheless, despite these differences, the comparison is a useful check.

BEDISK predicts a density-weighted average temperature, defined as

$$\overline{T}_{\rho} \equiv \frac{1}{M} \int_{\text{Disk}} T \rho dV, \quad (19)$$

(where M is the total mass of the disk), of 11 300 K. This is to be compared to the 14 500 K quoted by MM (in their Table 1). This significant difference is simply one of definition: the density-weighted average quoted by MM is actually defined as $(\sum \rho_{ij} T_{ij}) / \sum \rho_{ij}$ where the sum is over all of the grid points in the calculation. Computing this quantity for the current BEDISK model yields 13 900 K which agrees with the MM result to within 5%.

Figure 1 compares the ratio of the BEDISK temperature to the MM temperature throughout the entire circumstellar disk. Agreement is generally good; BEDISK tends to be somewhat cooler near the equatorial plane in the inner portion of the disk, while somewhat hotter towards the upper edge. However, 80% of the grid points agree to within $\pm 20\%$. The largest differences tend to occur along with upper edge of the envelope where the optical depths (to the nearest vertical edge of the disk) are most rapidly changing. The treatment of the escape of line radiation, as noted above, and particularly of how the OTS approximation was implemented (MM applied OTS to the whole disk as opposed to including an optical depth dependence as in equation 9), are likely the origin of the more significant differences.

3.2. Effect of Adding Metals on the Thermal Structure

Table 4 gives the disk parameters for 16 disk models computed to compare with observations of γ Cas. These models span a range of nearly two orders of magnitude in density (as obtained by varying ρ_o from $2.5 \cdot 10^{-12}$ to $1.0 \cdot 10^{-10} \text{ gm cm}^{-3}$) with two values assumed for the radial drop-off of the density in the equatorial plane, $R^{-2.5}$ and $R^{-3.5}$. All models assumed $T_o = 13500$ K for the isothermal temperature which sets the vertical density scale-height via Eq. 3. Also given in the table are the predicted density-weighted temperatures, the disk emission measures (in cm^{-3}), defined as

$$\text{EM} \equiv \int_{\text{Disk}} n_e^2 dV, \quad (20)$$

and the predicted total H α luminosities (in erg s^{-1}). Section 3.3 discusses how the H α luminosity was com-

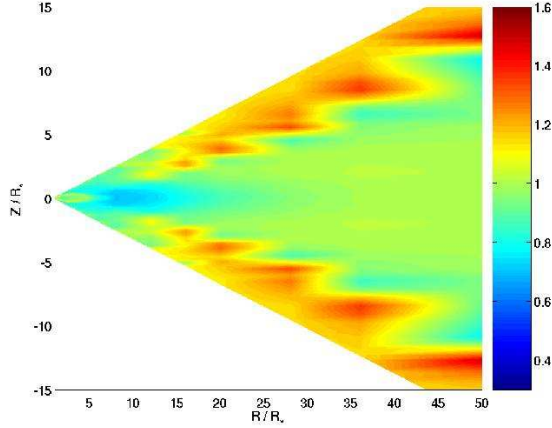


FIG. 1.— Ratio of the BEDISK temperature to the MM temperature for γ Cas.

TABLE 4
MODEL DISK PARAMETERS.

n	ρ_o g cm^{-3}	\bar{T}_ρ K	log EM cm^{-3}	log H α erg s^{-1}
2.5	$2.5 \cdot 10^{-12}$	14060	59.25	33.43
2.5	$5.0 \cdot 10^{-12}$	12870	59.84	33.79
2.5	$7.5 \cdot 10^{-12}$	12420	60.16	33.99
2.5	$1.0 \cdot 10^{-11}$	12170	60.40	34.12
2.5	$2.5 \cdot 10^{-11}$	11040	61.10	34.48
2.5	$5.0 \cdot 10^{-11}$	9420	61.50	34.69
2.5	$7.5 \cdot 10^{-11}$	8590	61.57	34.77
2.5	$1.0 \cdot 10^{-10}$	8140	61.62	34.80
3.5	$2.5 \cdot 10^{-12}$	13990	58.88	32.90
3.5	$5.0 \cdot 10^{-12}$	13740	59.48	33.17
3.5	$7.5 \cdot 10^{-12}$	13500	59.81	33.31
3.5	$1.0 \cdot 10^{-11}$	13290	60.05	33.40
3.5	$2.5 \cdot 10^{-11}$	12080	60.82	33.68
3.5	$5.0 \cdot 10^{-11}$	11050	61.35	33.85
3.5	$7.5 \cdot 10^{-11}$	10560	61.48	33.95
3.5	$1.0 \cdot 10^{-10}$	10240	61.55	34.01

puted. The parameters of the central star were again those of Table 3.

The density-weighted temperatures predicted by the models are plotted in Figure 2 as a function of ρ_o . These results are compared to the predicted density-weighted temperatures for a set of pure hydrogen disks with identical physical parameters. Also shown in the Figure is the observed disk temperature for γ Cas of 9500 ± 1000 K as found by Hony et al. (2000) by fitting the IR Humphrey’s bound-free jump at $3.4 \mu\text{m}$. As expected, denser disks predict lower density-weighted temperatures.

The $R^{-2.5}$ models are consistent with the Hony et al. (2000) result for densities in the range of 3 to $8 \cdot 10^{-11} \text{ g cm}^{-3}$. This agrees well with the density estimated by Hony et al. (2000) using their observations and the disk models of Waters (1986). The $R^{-3.5}$ models are only just consistent with the Hony et al. (2000) result for largest densities considered, $\rho_o \approx 10^{-11} \text{ g cm}^{-3}$.

The predicted temperature trend as a function of ρ_o has an interesting dependence on the metallicity of the gas. For low density disks, the solar composition disks are considerably cooler than the pure hydrogen models by 1-2000 K. However, the difference decreases for higher

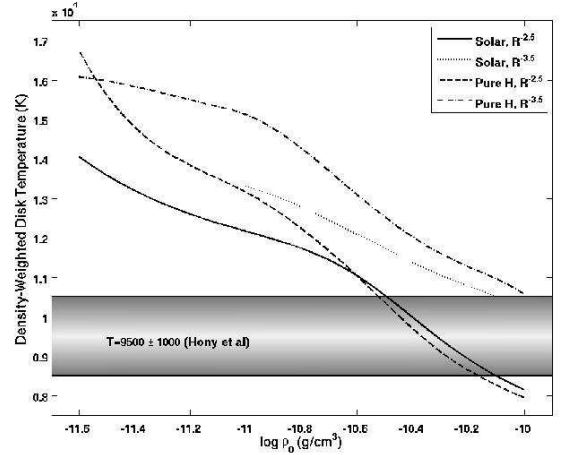


FIG. 2.— Density-weighted disk temperatures for the models of Table 4.

disk densities, $\rho_o > 2 \cdot 10^{-11} \text{ g cm}^{-3}$. Indeed, for the $R^{-2.5}$ models, the higher density solar and pure hydrogen disks predict nearly the same density-weighted temperatures. This behaviour can be understood in terms of the heating and cooling avenues introduced by metals. Metals can act to cool the gas due to the escape of collisionally-excited line radiation. However, metals can also help to heat the gas via photoionization. If the optical depths in the hydrogen continua (excluding the Lyman continuum) are low, then the additional heating provided by the photoionization of metals is negligible in comparison to hydrogen. In this case, it is the cooling due to collisionally-excited line radiation that dominates. In a low-density disk, line cooling is further enhanced by the small optical depths (and hence high escape-probabilities) in the lines.

At high densities, however, the optical depths in the hydrogen bound-free continua are much larger; photoionization heating due to metals can then become important, particularly as many abundant metals have bound-free thresholds in the short-wavelength region of the Balmer continuum which is near the photospheric flux maximum in B stars. In this case, metals add both heating and cooling and the net result is a very similar density-weighted temperature to the case of a pure hydrogen plasma. These trends help explain why (Millar & Marlborough 1998) were able to obtain a reasonable density-weighted temperature for γ Cas despite using a pure hydrogen envelope.

Two-dimensional temperature distributions in the disk for several different density $R^{-2.5}$ models are shown in Figure 3. The inner portion of the disk for $R/R_* < 5$ is expanded in each case for clarity. These figures clearly show the development of a cool region near and in the equatorial plane for the higher density disks. These denser disks have fairly strong vertical temperature gradients perpendicular to the equatorial plane. Given this, it would seem prudent to re-integrate the equation of hydrostatic equilibrium at each radial distance, accounting for the vertical variation of the gas temperature, and then to iterate the pressure structure along with the thermal solution to produce a disk that is in both radiative and (vertical) hydrostatic equilibrium; we shall present such models in a future work (McGill, Sigut & Jones 2006). However, as the focus of the present work is on the ther-

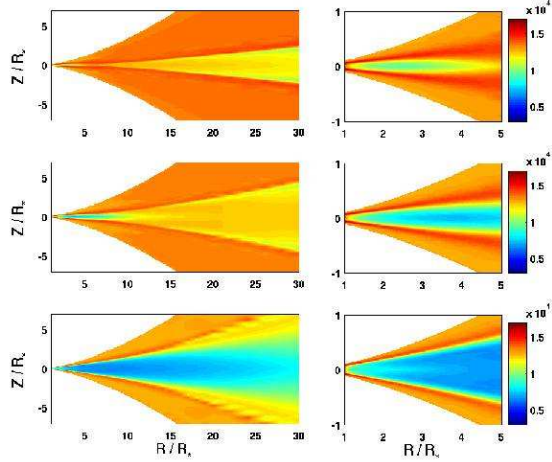


FIG. 3.— Circumstellar disk temperature as predicted by three $R^{-2.5}$ models. The top panel has $\rho_o = 1 \cdot 10^{-12} \text{ g cm}^{-3}$, the middle panel, $\rho_o = 5 \cdot 10^{-12}$, and the bottom panel, $\rho_o = 5 \cdot 10^{-11}$. Each panel on the right enlarges the inner portion of the disk from the panel on its left.

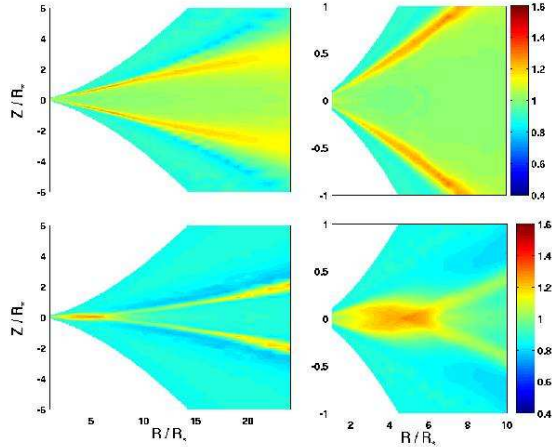


FIG. 4.— Temperature ratio between a full solar composition disk to that of a pure hydrogen disk. Shown in the bottom panel is a model with $\rho_o = 5 \cdot 10^{-12} \text{ g cm}^{-3}$, and in the top panel, one with $\rho_o = 5 \cdot 10^{-11} \text{ g cm}^{-3}$. Both models had an $R^{-2.5}$ density drop-off in the equatorial plane. Each panel on the right enlarges the inner portion of the disk from the panel on its left.

mal structure of the disk, it is convenient to have a fixed density structure so that the thermal effect of the gas metallicity can be unambiguously seen.

Figure 4 presents a detailed comparison of the temperature structure predicted by a gas with a realistic solar composition to that of a pure hydrogen model. The figure compares the temperature ratio $T^{\text{Solar}}/T^{\text{PureH}}$ for two densities, $\rho_o = 5 \cdot 10^{-11}$ and $\rho_o = 5 \cdot 10^{-12} \text{ g cm}^{-3}$. In both cases, the optically thin gas far above the equatorial plane is cooler with the inclusion of metals. However, in the lower density model, $\rho_o = 5 \cdot 10^{-12} \text{ g cm}^{-3}$, the gas in the equatorial plane near the star is hotter for the solar composition gas out to $R/R_* \sim 6$. In the higher density model, the gas near the equatorial plane has nearly the same temperature in the solar and pure hydrogen models. These trends are consistent with the effects noted in the discussion of the density-weighted average disk temperatures.

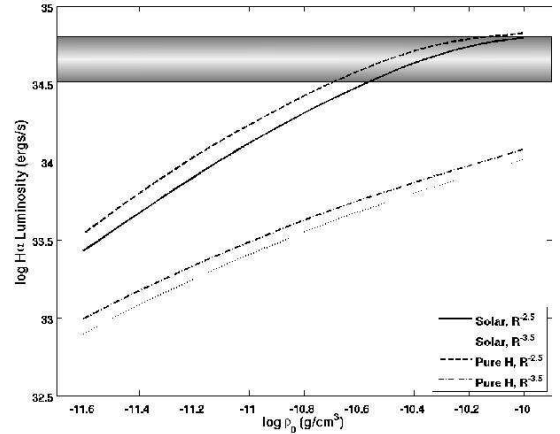


FIG. 5.— The predicted energy loss in $\text{H}\alpha$ from Eq. 21 (in ergs s^{-1}) for the models of Table 4. Shown as the shaded rectangle is the observed range of values from Kastner & Mazzli (1989) and (Stee et al. 1995).

3.3. Line Luminosities

Figure 5 plots the total energy lost in $\text{H}\alpha$ (in ergs s^{-1}) by the 16 models of Table 4. The line luminosity was found by integrating the flux divergence, in the escape probability approximation², over the volume of the disk, *i.e.*

$$L = h\nu_{ij} A_{ji} \int_{\text{Disk}} n_j P_{\text{esc}}(\tau_{ij}) dV. \quad (21)$$

For $\text{H}\alpha$, i is level $n = 2$ of H I and j is level $n = 3$. Also shown in the Figure is the $\text{H}\alpha$ luminosity observationally determined by Kastner & Mazzli (1989) and Stee et al. (1995). The $\text{H}\alpha$ luminosity from γ Cas is known to be variable, but the cited values are typical of the current epoch. There is good agreement with the observed luminosity for $R^{-2.5}$ models with ρ_o between $2.5 \cdot 10^{-11}$ and $10^{-11} \text{ g cm}^{-3}$. This result is consistent with the models that best fit the observed disk temperature of Hony et al. (2000). However, the $R^{-3.5}$ models seem inconsistent with the total energy loss in $\text{H}\alpha$ for the range of disk densities considered.

Figure 6 shows energy escaping in all of the included radiative transitions for the $R^{-2.5}$ model with $\rho_o = 5 \cdot 10^{-11} \text{ g cm}^{-3}$. The fluxes are again found by integrating Eq. 21 over the disk. It is important to keep in mind that Figure 6 is not a spectrum (which would be obtained by integrating the transfer equation along a series of rays through the computational domain); it is simply a plot of the energy loss per second in each line acting to cool the gas. Nevertheless, it gives a good indication of the expected strong emission lines in the disk spectrum. For this particular model, 94% of the energy loss is provided by the lines of H I . Contributing at the level of $\approx 1\%$ percent are Fe II , C II , Mg II , and He I . Next to the lines of H I , the largest energy losses are in the resonance lines $\lambda 1333.6 \text{ \AA}$ line of C II ($2s^2 2p^2 P^\circ - 2s 2p^2 D$) and the h and k lines of Mg II near $\lambda 2800 \text{ \AA}$. Although it does not possess a single strong line, cooling due to Fe II dominates over all of the metals due to its rich spectrum with many collisionally-excited lines. It should be noted that Figure 6 and the percentage contributions cited above

² In the escape probability approximation, the net radiative bracket is replaced by the (single-flight) escape probability.

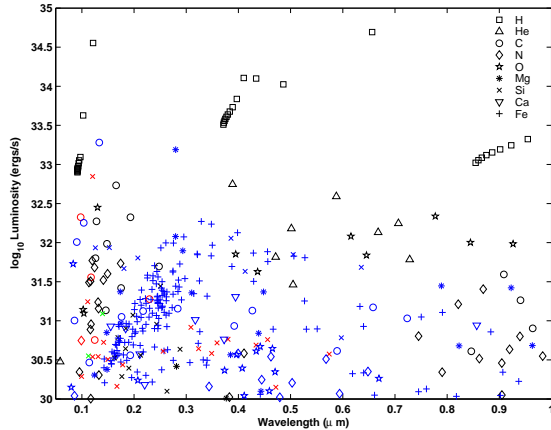


FIG. 6.— The energy loss in each radiative transition predicted by the $R^{-2.5}$ disk model with $\rho_o = 5 \cdot 10^{-11} \text{ g cm}^{-3}$. Only transitions with an energy loss above $10^{30} \text{ erg s}^{-1}$ are shown. The symbols representing the various elements are as indicated in the legend. The ionization stage is coded by colour: neutral (black), first ion (blue), second ion (red), third ion (green).

represent a *global* picture of energy loss integrated over the entire disk. The impact of the heating and cooling contributions of metals can be much larger at individual grid locations as demonstrated by Figure 4.

3.4. Predicted IR spectral energy distributions

In this section, we consider the predicted IR continuum energy distribution as emitted *perpendicular* to the disk³. Such models have a zero inclination angle between the rotation axis and the observer's line of sight. This spectrum is easily found by solving the radiative transfer equation vertically through the disk at each R_i . If $I_i \equiv I_{+1,\nu}(R_i)$ is the emergent intensity for the annulus of area $A_i = \pi(R_{i+1/2}^2 - R_{i-1/2}^2)$ then the SED seen by the observer will be

$$L_{\nu}^{\text{Star+Disk}} = I_{\nu}^* \pi R_*^2 + \sum_{i=1}^{n_R} I_i A_i. \quad (22)$$

Here R_* is the radius of the star, I_{ν}^* is the specific intensity corresponding to the stellar surface, and I_i is the specific intensity of the i^{th} disk annulus. It is well known that at IR wavelengths, Be stars possess an excess of radiation over that predicted by an appropriate stellar photosphere model (Coté & Waters 1987). This excess comes mainly from free-free emission in the ionized disk⁴, with a small contribution from free-bound emission shortward (in wavelength) of the ionization edges.

The near-IR spectral energy distributions are shown in Figure 7 for the $R^{-2.5}$ models of Table 4. Plotted is the (monochromatic) IR excess expressed in magnitudes,

$$Z_{\nu} \equiv 2.5 \log \left(\frac{L_{\nu}^{\text{Star+Disk}}}{L_{\nu}^{\text{Star}}} \right). \quad (23)$$

The discontinuous jumps at wavelengths less than $5 \mu\text{m}$ in this figure, particularly for higher densities, represent the hydrogen free-bound continua for recombination to $n = 4$ ($1.4 \mu\text{m}$) and $n = 5$ ($2.2 \mu\text{m}$). Unlike

³ We shall present detailed synthesis for the infrared hydrogen disk spectrum for arbitrary inclination angles in a future work.

⁴ Note that the exact expression for the free-free Gaunt factor was used for this calculation.

(plane-parallel) stellar photospheres which have bound-free edges in absorption (reflecting the inward increase in temperature), circumstellar material exhibits the bound-free edges in emission, reflecting the increase in the gas emissivity due to recombination. Thus the figure indicates a small contribution from free-bound emission to the infrared excess at these wavelengths. We also note that as the disk density is increased, the infrared excess steepens most strongly between the wavelengths of 1 and $5 \mu\text{m}$.

To compare with observations, we first show the 12 and $25 \mu\text{m}$ IRAS IR excesses for γ Cas found by Coté & Waters (1987). The model that best matches the IRAS IR excess at these wavelengths has a slightly smaller density, $\rho_o \approx 10^{-11} \text{ g cm}^{-3}$, than the model that best matches the observed average disk temperature and energy loss in $\text{H}\alpha$, $\rho_o \approx 3 \cdot 10^{-11} \text{ g cm}^{-3}$ (Figure 2). However, there is good evidence that γ Cas is seen at an inclination of $i > \approx 55^\circ$ (Tycner et al. 2006), as opposed to being viewed pole-on ($i = 0^\circ$) as assumed by the models. Hence the models have an effective emitting area that is too large and the IR excess is likely overestimated. In addition, the spectra for non-zero inclination angles will reflect the contribution of a different set of rays passing through the disk; the different physical conditions along these rays will lead to differences in the gas opacity and emissivity and hence a different predicted intensity along each ray.

We also show in Figure 7 the 2.5 to $11.6 \mu\text{m}$ Infrared Space Observatory (ISO) spectrophotometry⁵ for γ Cas. In order to compare the ISO fluxes at the Earth to our photospheric model (to set the reference flux to extract the excess), we require the angular diameter of the star. Tycner et al. (2005) cite the major axis of the $\text{H}\alpha$ emitting region of γ Cas of 3.67 ± 0.09 milli-arcseconds, but this has a large contribution from the circumstellar disk. To resolve this problem, we have chosen an angular diameter such that the ISO data reproduces the $12 \mu\text{m}$ IRAS excess. Combining this stellar angular diameter for γ Cas with the range of Hipparcos distances listed in Table 3, we find a required radius for γ Cas of between 6.8 and 8.4 solar radii. While this result in disagreement with the 10 solar radii listed in Table 3, the larger value is within the plausible error range for γ Cas's radius. With this normalization, the ISO observations match reasonably well with the $\rho_o \approx 10^{-11} \text{ g cm}^{-3}$ model prediction over the considered wavelength range. The fit is actually worse closer to the normalization point; the shorter wavelength excess, between $2.5 < \lambda < 5 \mu\text{m}$, is quite well reproduced. Similar caveats to those ending the previous paragraph apply here: a detailed comparison will be made with a model that correctly accounts for the viewing inclination of γ Cas in a future work.

3.5. An Approximate Treatment of the Diffuse Radiation Field

While the OTS approximation is simplest treatment of the diffuse radiation field, Figure 3 shows that in the densest disks ($\rho_o \approx 5 \cdot 10^{-11} \text{ g cm}^{-3}$), grid locations near the equatorial plane can become quite cool due to large

⁵ We have extracted this data from the ISO on-line archive. The spectrophotometry is from the PHT-40 instrument for observing series TDT 76803401.

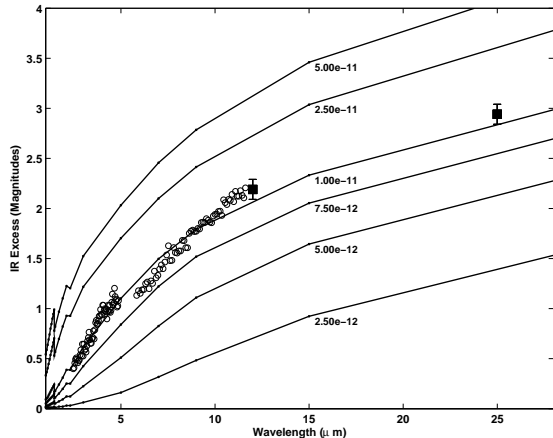


FIG. 7.— The IR excess expressed in magnitudes predicted by the $R^{-2.5}$ models of Table 4. The square data points at 12 and 25 μm are from Côté & Waters (1987). The open circles are the ISO spectrophotometry.

optical depths back to the central star. However, examining the thermal structure in the Z -direction at such a location typically shows that at heights above and below the equatorial plane, the gas can still be quite hot as it can be directly illuminated by at least a portion of the star. One might expect that the radiation emitted from these hot “sheaths” might be an important source of secondary photoionizing radiation for the equatorial gas (Carciofi & Bjorkman 2006).

In principle, the calculation of J_{ν}^{Dif} in Eq. 5 requires a solution of the transfer equation in the 2D cylindrical geometry⁶. However, to estimate the potential effect of this diffuse field on the current work, we have tried a simpler and approximate approach. We solve, at each R_i , the radiative transfer equation perpendicular to the disk in the Z -direction using the method of short-characteristics (Olson & Kunasz 1987). The mean intensity along this ray is then

$$J_{\nu}(Z_j) = \frac{1}{2} \{I_{\mu=+1,\nu}(Z_j) + I_{\mu=-1,\nu}(Z_j)\}. \quad (24)$$

For this solution, zero incident radiation is assumed perpendicular to the disk. We then estimate the diffuse contribution to the photoionizing radiation field at each Z_j by assigning

$$J_{\nu}^{\text{Dif}}(Z_j) = W_{\text{dif}} J_{\nu}(Z_j), \quad (25)$$

Here W_{dif} represents an ad-hoc dilution factor, between zero and one, for the perpendicular rays. The expectation is that J_{ν}^{Dif} will potentially be most important in the cool equatorial regions that develop for higher density disks such as the one illustrated in the bottom panel of Figure 3. In such a cool obscured region, the hot sheaths above and below cover approximately 1/2 of the available 4π steradians so a dilution factor of $W_{\text{dif}} = 0.5$ is a reasonable approximation. In regions of the disk where the central star is not obscured, the choice of W_{dif} is irrelevant as $J^{\text{Dir}} \gg J^{\text{Dif}}$. For this reason, we have taken W_{dif} to be 1/2 at all grid locations in the disk.

⁶ A direct implementation of this approach can be found in Carciofi & Bjorkman (2006) who use a Monte Carlo approach to radiative transfer to estimate the diffuse radiation field in the envelope of a somewhat later-type Be star.

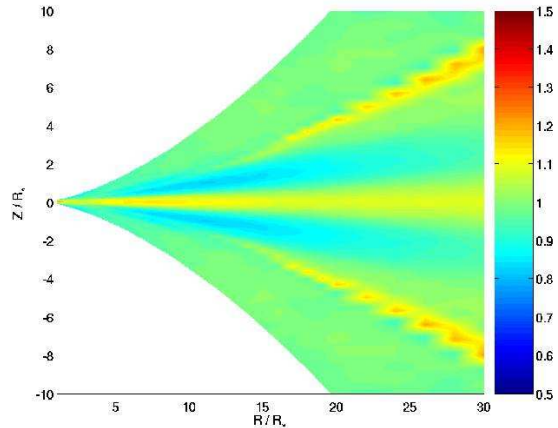


FIG. 8.— The effect of adding the diffuse contribution of Eq. 25 to the temperatures predicted for the $R^{-2.5}$ disk model with $\rho_o = 5 \cdot 10^{-11} \text{ g cm}^{-3}$. Plotted is the temperature ratio of a calculation including Eq. 25 to one omitting this contribution.

Figure 8 shows the effect of adding such an approximate treatment of J^{Dif} to the $R^{-2.5}$ disk model with $\rho_o = 5 \cdot 10^{-11} \text{ g cm}^{-3}$, the model which best matched the observed disk temperature and the total $\text{H}\alpha$ luminosity. With the diffuse field added, the amount of additional heating in the equatorial plane is fairly small, with only a 10 – 20% increase in the temperature there. Hence, we feel that the previously computed models are reliable despite the approximate treatment of the diffuse field through the OTS approximation.

Note that this figure is not meant to imply that the effect of the diffuse field is negligible; in both runs, the on-the-stop (OTS) approximation, which approximates the local trapping of radiation with $\lambda < 912 \text{ \AA}$ and hence the diffuse photoionizing radiation field for $\lambda < 912 \text{ \AA}$ was employed following Eq. 9. If the OTS approximation is turned off, there is considerable cooling of the equatorial regions⁷ (see also Millar & Marlborough 1999) and this would mask the effect (illumination of these same regions from above and below) that we were trying to investigate.

4. CONCLUSIONS

For the first time, we have constructed radiative equilibrium models for the disk of γ Cas using a gas with a solar chemical composition. We find that a model with a power-law equatorial gas density of $\rho(R) \approx 3$ to $5 \cdot 10^{-11} (R/R_*)^{-2.5} \text{ g cm}^{-3}$, which is in vertical (isothermal) hydrostatic equilibrium, can reproduce several overall observed disk properties, including its (density-weighted) average temperature, the energy loss in $\text{H}\alpha$, and the near infrared flux excess.

Also in this work, we have investigated the differences between our solar composition radiative equilibrium models and the corresponding set of pure hydrogen models with the same disk parameters. The effect of the additional heating and cooling provided by elements heavier than hydrogen on global measures of the disk structure, such as the density-weighted average disk temperature or the total energy loss in $\text{H}\alpha$, depend strongly

⁷ A subtle point is whether a model including J^{Dif} according to Eq. 25 should also employ the OTS approximation. In principle, employing both over counts the local radiation field in each volume element.

on the parameter ρ_o (the assumed equatorial density near the stellar surface) which sets the overall density of the disk. For low disk densities, $\rho_o < 10^{-11} \text{ g cm}^{-3}$, the density-weighted averaged disk temperature is generally 1–2000 K cooler with a solar composition, due mostly to enhanced collisionally-excited line cooling. At higher densities, absorption of ionizing radiation in the bound-free continua of elements heavier than hydrogen provides additional heating which offsets somewhat the additional line cooling.

In examining the detailed temperature at each position within the disk, differences of up to $\approx \pm 40\%$ are found in comparing the solar composition models to the pure hydrogen models. While the global energy loss in H α in the solar and pure hydrogen models is similar, these significant differences in the disk temperature distribution may manifest themselves in the detailed spectra. The next step in the comparison between these two sets of models is to present predicted spectra over a wide range of wavelengths for a wide range of viewing inclinations.

The BEDISK code represents a compromise between computational efficiency and realism. The code's most notable approximations are the treatment of the disk diffuse radiation field, the use of (first-order) static, escape probabilities for the line radiative transfer, the assumption of a spherical, non-rotating, central star, and the somewhat limited atomic models. Nevertheless, these approximations allow the code to efficiently explore a wide

region of parameter space for the thermal structure of the circumstellar disks surrounding hot stars. Future work will proceed along two fronts: we will use the current version of BEDISK to compute a series of Be disk thermal models that will serve as the basis for detailed spectral synthesis to produce line profiles, interferometric visibilities, and continuum polarization signatures which can be directly compared to observations. Along the second front, we shall improve some of the basic assumptions of the code. Most notably, we will enforce a vertical hydrostatic equilibrium density structure consistent with the thermal solution, allow for potential gravitational darkening (and geometric distortion) of the central star by rapid rotation, and account for the diffuse photoionizing radiation field from the disk by a direct solution of the 2-D radiative transfer problem.

We would like to thank Chris Tycner for many helpful discussions. We thank Rens Waters for clarifying the IR excess of γ Cas. We also thank Kyle Lawson, Anna Molak, and Laura Thomson for help as part of their NSERC Summer Student awards. Finally, we would like to thank the anonymous referee for a careful reading of the text and providing many helpful comments and suggestions. This work is supported by the Canadian Natural Sciences and Engineering Research Council through Discovery Grants to TAAS and CEJ.

APPENDIX

THE ATOMIC DATA

Energy levels for all atoms and ions were adopted from the NIST Atomic Spectra Database⁸. Radiative transition probabilities and photoionization cross sections were adopted from the Opacity Project Database TOPbase⁹. The photoionization cross sections, which include complex resonance features due to autoionization, were smoothed by convolution with a Gaussian down to the resolution of the ATLAS frequency grid. Thermally-averaged collision strengths for the electron impact excitation of hydrogen were adopted from Callaway (1994), Aggarwal et al. (1991), and Chang, Avrett & Loeser (1991). Thermally-averaged collisional strengths for the remaining atoms and ions were adopted from the compilation of Pradhan & Peng (1995) where available. The Gaunt factor approximation was used for the remaining dipole-allowed transitions. The atomic data for iron and its ions were adopted from the extensive model atoms constructed by Sigut & Pradhan (2003) and Sigut, Pradhan & Nahar (2004).

REFERENCES

- Aggarwal, K.M., Berrington, K.A., Burkner, P.G., & Pathak, A. 1991 *J. Phys. B: At. Mol. Opt. Phys.* 24, 1385
- Anders, E., & Grevesse, N. 1989 *Geochim. Cosmochim. Acta.* 53, 197
- Anders, E., & Grevesse, N. 1993 *Physica Scripta* T47, 133
- Callaway, J. 1994 *Atomic Data & Nuclear Data Tables*, 57, 9
- Cannon, C.J. 1985 *The Transfer of Spectral Line Radiation* (Cambridge University Press: Cambridge)
- Carciofi, A. C., & Bjorkman, J. E. 2005, *ApJ*, 639, 1081
- Chang, E.S., Avrett, E.H., & Loeser, R. 1991 *A&A*, 247, 580.
- Coté, J., & Waters, L. B. F. M. 1987, *A&A*, 176, 93
- Coyne, G. V., & Kruszewski, A. 1969, *AJ*, 74, 528
- Cranmer, S. R. 2005, *ApJ*, 634, 585
- Dougherty, S. M., & Taylor, A. R. 1992, *Nature*, 359, 808
- Fremat, Y., Zorec, J., Hubert, A.-M., & Floquet, M. 2005 *A&A*, 440, 305
- Hony, S., Waters, L.B.F.M., Zaai, P.A., de Koter, A., Marlborough, J.M., Millar, C.E., Trams, N.R., Morris, P.W., & de Graauw, Th. 2000 *A&A*, 355, 187
- Harmanec, P., & 10 co-authors 2000 *A&A*, 364, L85
- Hubeny, I., Hummer, D.G., & Lanz, T. 1994 *A&A*, 282, 151
- Jones, C. E., Sigut, T. A. A., & Marlborough, J. M. 2004, *MNRAS*, 352, 841
- Kastner, J.H., & Mazzli, P.A. 1989 *A&A*, 210, 295
- Kurucz, R. F. 1993, Kurucz CD-ROM No. 13. Cambridge, Mass: Smithsonian Astrophysical Observatory
- Lee, Saio, & Osaki 1991 *MNRAS*, 250, 432
- Limber, D. N. 1969, *ApJ*, 157, 785
- Marlborough, J. M. 1969 *ApJ*, 156, 135
- McAlister, H. A., Brummelaar, T. A., Gies, D. R., Huang, W., Bagnuolo, W. G., Jr., Shure, M. A., Sturmman, J., Sturmman, L., Turner, N. H., Taylor, S. F., & 6 co-authors 2005, *ApJ*, 628, 439
- McGill, M. A. Sigut, T.A.A., & Jones, C.E., 2006 American Astronomical Sociey Meeting 208
- Mihalas, D. 1978 *Stellar Atmospheres* (W. H. Freeman & Company: New York)
- Millar, C. E., & Marlborough, J. M. 1999, *ApJ*, 516, 276
- Millar, C. E., & Marlborough, J. M. 1998, *ApJ*, 494, 715
- Miroshnichenko, A. S, Bjorkman, K. S, & Krugov, V. D. 2002, *PASP*, 114, 1226
- Moore, C. E., & Merrill, P. W. 1968 *Partial Grotrian Diagrams of Astrophysical Interest*, NSRDS-NBS 23
- Netzer, H. 1990 *Active Galactic Nuclei: SAAS-FEE Advanced Course 20 Lecture Notes*, R.D. Blandford & H. Netzer editors, (Springer-Verlag, Berlin), 57

⁸ <http://units.nist.gov/PhysRefData/ASD/index.html>

⁹ <http://cdsweb.u-strasbg.fr/topbase.html>

- Olson, G. L., & Kunasz, P. B. 1987 JQSRT, 38, 325
- Osterbrock, D. E. 1989, *Astrophysics of Gaseous Nebulae and Active Galactic Nuclei* (Mill Valley: Univ. Sci. Books)
- Owocki, S. P. 2004, in IAU Symposium 215, *Rotation and Mass Ejection: the Launching of Be-Star Disks* ed. A. Maeder, & P. Eenens (San Francisco: ASP), 515
- Perryman, M.A.C., & ESA. 1997 *The Hipparcos and Tycho Catalogues*, (ESA SP-1200; Noordwijk: ESA)
- Poeckert, R., & Marlborough, J. M. 1978, ApJ, 220, 940, PM
- Porter, J. M. 1999, A&A, 348, 512
- Porter, J. M., & Rivinius, T. 2003, PASP, 115, 1153
- Pradhan, A.K., & Peng, J. 1995 in *The Analysis of Emission Lines*, Space Telescope Science Symposium Series 8, R.E. Williams & M. Livo editors, (Cambridge University Press), 8
- Quirrenbach, A., Bjorkman, K. S., Bjorkman, J. E., Hummel, C. A., Buscher, D. F., Armstrong, J. T., Mozurkewich, D., Elias, N. M. II, & Babler, B. L. 1997, ApJ, 479, 477
- Quirrenbach, A., Hummel, C. A., Buscher, D. F., Armstrong, J. T., Mozurkewich, D., & Elias, N. M. II 1993, ApJ, 416, L25
- Rybicki, G. B., & Lightman, A. P. 1979 *Radiative Processes in Astrophysics* (John Wiley & Sons: New York)
- Sigut, T.A.A 1996, ApJ, 473, 452
- Sigut, T.A.A, & Pradhan, A.K. 2003, ApJS, 145,15
- Sigut, T.A.A, Pradhan, A.K., & Nahar, S. N. 2004, ApJ, 611, 81
- Smith, Myron A., Cohen, David H., Gu, Ming Feng, Robinson, Richard D., Evans, Nancy Ramage, & Schran, Prudence G.2004, ApJ, 600,972
- Stee, P., de Araujo, F. X., Vakili, F., Mourard, D. Arnold, L., Bonneau, D., Morand, F., & Tallon-Bosc, I. 1995, A&A, 300, 219
- Struve, O. 1931, ApJ, 73, 94
- Tielens, A. G. G. M. *The Physics and Chemistry of the Interstellar Medium*, Cambridge University Press
- Townsend, R. H. D., Owocki, S. P., & Howarth, I. D. 2004 MNRAS, 350, 189
- Tycner, Christopher, Lester, John B., Hajian, Arsen R., Armstrong, J. T., Benson, J. A., Gilbreath, G. C., Hutter, D. J., Pauls, T. A., & White N. M 2005, ApJ, 624, 359
- Tycner, Christopher, Gilbreath, G. C., Zavala, R. T., Armstrong, J. T., Benson, J. A., Hajian, Arsen R., Hutter, D. J., Jones, C. E., Pauls, T. A., & White, N. M. 2006, AJ, 131, 2710
- Wade, R.A., & Rucinski, S.M. 1985 A&A, 60, 471
- Waters, L. B. F. M. 1986 A&A, 162, 121
- Waters, L. B. F. M., Cote, J., & Lamers, H. J. G. L. M. 1987, A&A, 185, 206
- Waters, L. B. F. M., & Marlborough, J. M. 1992 A&A256, 195
- Wood K., Bjorkman K. S., & Bjorkman J. E. 1997, ApJ, 477, 926